PAPER PRESENTED AT ECCOMAS 2012 - MULTIPHYS-BME

Capillary networks in tumor angiogenesis: From discrete endothelial cells to phase-field averaged descriptions via isogeometric analysis

Guillermo Vilanova[*,†], Ignasi Colominas and Hector Gomez

Department of Applied Mathematics, University of A Coruña, Campus de Elviña, 15071, A Coruña, Spain

SUMMARY

Tumor angiogenesis, the growth of new capillaries from preexisting ones promoted by the starvation and hypoxia of cancerous cell, creates complex biological patterns. These patterns are captured by a hybrid model that involves high-order partial differential equations coupled with mobile, agent-based components. The continuous equations of the model rely on the phase-field method to describe the intricate interfaces between the vasculature and the host tissue. The discrete equations are posed on a cellular scale and treat tip endothelial cells as mobile agents. Here, we put the model into a coherent mathematical and algorithmic framework and introduce a numerical method based on isogeometric analysis that couples the discrete and continuous descriptions of the theory. Using our algorithms, we perform numerical simulations that show the development of the vasculature around a tumor. The new method permitted us to perform a parametric study of the model. Furthermore, we investigate different initial configurations to study the growth of the new capillaries. The simulations illustrate the accuracy and efficiency of our numerical method and provide insight into the dynamics of the governing equations as well as into the underlying physical phenomenon. Copyright © 2013 John Wiley & Sons, Ltd.

1. INTRODUCTION

Angiogenesis is one of the processes of creation of new blood vessels in the human organism. Unlike vasculogenesis, which depends upon precursor cells [1], or intussusceptive angiogenesis, which splits blood vessels [2], angiogenesis is the process by which new blood vessels are formed from preexisting ones through migration and proliferation mechanisms [3]. This biological phenomenon is observed in primary phases of the human life, especially during the embryo development [4]. Thereafter, in the adult life, it only appears in very specific events and only for a short period, typically in the time scale of days or weeks. For example, it is present in wound healing, where the increment in the demand of nutrients and oxygen by dividing cells is satisfied through the creation of new blood vessels [5]. Several diseases are related to a deregulation of angiogenesis, such as chronic wounds, diabetic retinopathy, atherosclerosis, ischemic heart and limb disease, and cancer [6]. Here, we focus on cancer-induced angiogenesis.

---

*Correspondence to: Guillermo Vilanova, Department of Applied Mathematics, University of A Coruña, Campus de Elviña, 15071, A Coruña, Spain.

[†]E-mail: gvilanovac@udc.es

1.1. Tumor angiogenesis and its key role in cancer growth

Certain types of cancer form solid tumors of aberrant, mutated cells. These cells, which proliferate in a high-rate manner, aggregate in solid masses that grow, consuming the resources of the surroundings. When the tumor has grown up to a certain size, not larger than 2 mm radius in experiments [7], its global growth stops. This occurs because of the scarceness of nourishment and oxygen, which does not even cover the demands for maintaining the basic cell processes in the core of the mass. Tumors only grow further if the cancerous cells acquire through mutations one of the so-called hallmarks of cancer [8, 9]: the ability to induce angiogenesis. The hypoxic cells (HYCs) surrounding the tumor core (even many malign-induced, non-cancerous cells from the tumor micro-environment, such as inflammatory cells) gain the capacity to release tumor angiogenic factors (TAFs) that counterbalance the existent angiogenic factor equilibrium. As a result, the growth of new capillaries is promoted towards the tumor, pervading the cell mass and nourishing the HYCs. Thus, angiogenesis enables a shift in tumor development endowing the neoplastic mass with nutrients and oxygen to grow without limits and with new ways of migration to other tissues or organs of the body.

1.2. Biological description of tumor angiogenesis

Angiogenesis is a complex phenomenon that may be described as a multistage process composed of the following steps: the activation, the initiation of the sprout, and the growth of the capillary. The tumor angiogenesis process is described in Figure 1 as a conceptual scheme. For a detailed description of the angiogenesis process, the reader is referred to [3] and the references therein. The activation starts when the equilibrium of the pro-angiogenic and anti-angiogenic factors is disturbed near the endothelial cells that compose the blood vessels. The disequilibrium may be caused by the arrival of tumor pro-angiogenic factor molecules that diffuse from the tumor and bind to the receptors of the endothelial cells. Those cells affected by the TAF are activated to become the leading cells of the incipient sprout: the tip endothelial cells (TECs). However, there is a mechanism that prevents the formation of several sprouts in the same region [10]. When several neighboring cells have the potential to become TECs, only one of them changes its phenotype to a migratory one becoming a TEC. Hereafter, the TEC segregates a ligand, namely delta-like ligand 4 (Dll-4), which pervades the cell's micro-environment and reaches the Notch 1 receptors of the neighboring cells, preventing them from becoming TECs and differentiating them into stalk endothelial cells (SECs), which acquire a proliferative phenotype. After activation of the TEC, the initiation of the new capillary starts. The TEC releases metalloproteinases (MMPs) degrading the basal lamina that envelops the vessel. In addition, they develop slender cytoplasmic protrusions, called filopodia, rich in receptors that enhance the detection of the stimuli that guide the migration [11]. The adjoining SECs follow the first movements of the TEC out of the capillary.

The growth of the capillary is guided by different mechanisms by means of the TEC, including, chemotaxis, haptotaxis, and mechanotaxis. The first refers to the movement towards a gradient of soluble molecules, in this case, TAF. The focal adhesion sites and the mechanical forces also contribute to establish the growth direction through haptotaxis and mechanotaxis, respectively. At the back of the TEC, the SECs are continuously dividing, stimulated by angiogenic factors. As the capillary grows, the endothelial cells form a lumen, allowing the blood to flow through them. Furthermore, they attract smooth muscle cells and pericytes, which provide support to the capillary, although at low levels in tumor capillaries. The growth continues until the lumina of two capillaries fuse, forming a loop that allows blood to flow. This phenomenon is called anastomosis. The growth may also be stopped if the driving stimuli end. In the case that concerns us, this point is reached when the hypoxic cancerous cells are supplied with enough nutrients and oxygen as to become normoxic. The capillaries promoted by tumors are usually slightly different from those created under normal circumstances [12]. Specifically, they become dependent on TAF presence; thus, when the stimuli are no longer present, the capillaries regress. In addition, the high pressure inside the tumor combined with the weakness of the vessels may make them collapse. Finally, the regrowth of the capillaries is common in tumor development, and it is carried out at a faster speed aided by the scaffold of basal lamina left behind by the regression of the vessels.
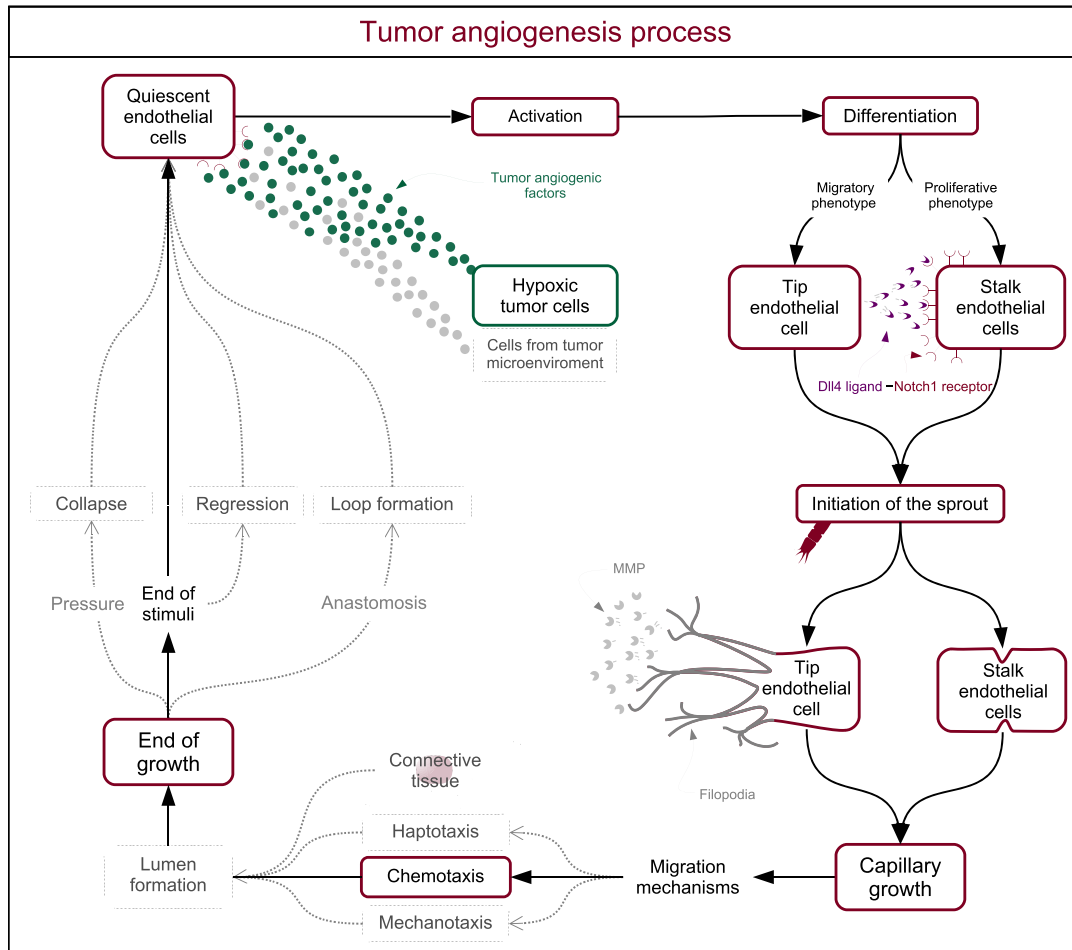
Figure 1. Conceptual scheme of the tumor angiogenesis process. The process starts on the top-left corner of the plot, when the quiescent endothelial cells become activated by tumor angiogenic factors. Thereafter, a series of events lead to the formation of new capillaries: the differentiation of the endothelial cells through the Delta–Notch signaling; the initiation of the sprout that breaks into the extracellular matrix; the capillary growth following different mechanisms; and the end of the growth. The mathematical model utilized in this paper accounts for all the phenomena in this figure, except those plotted with light gray fonts.

1.3. *Mathematical modeling of tumor angiogenesis*

Since Folkman hypothesized in 1971 that angiogenesis may play a key role in solid tumor growth [7], many research have focused on this phenomenon. A significant example is the development of new drugs that try to avoid the formation of new blood vessels in patients with cancer, such as angiostatin or Avastin [13]. Another example is the performance of *in vitro* or *in vivo* assays to study the role of particular mechanisms in angiogenesis, such as in the study of the mechanical forces in the direction of the capillary growth [14, 15]. Mathematical models have been proved to be valuable tools for the study of other diseases, such as cardiovascular diseases [16]. They provide the capacity to perform *in silico* simulations. In the literature, we found different mathematical approaches to tumor angiogenesis. Some of them rely upon continuous formulations [17–19], in which the blood vessels are described through the endothelial cell density that evolves in time according to a partial differential equation. Several phenomena determine the growth of the sprouts, such as the chemotaxis, the haptotaxis, or the random movement and proliferation of the endothelial cells. In addition, equations for the dynamics of the TAF or for the tumor progression complete the models. Other approach to tumor angiogenesis is to describe the activation, movement, and deactivation of the

TEC with a set of discrete rules [20–23]. These models include the migration through chemotaxis and haptotaxis, and the degradation of the extracellular matrix by the MMPs. This approach assumes that the SECs follow the path of the TEC, thus composing the new capillaries. Furthermore, some incorporate both the continuous and discrete descriptions into one model [24, 25], forming composite or hybrid models. They profit from the computational simplicity of continuous models and the ability to track individual components of the discrete descriptions. In them, the TEC is usually described as a discrete component, while the evolution of the SEC is governed by a differential equation. The hybrid model proposed by Travasso *et al.* [26] fits into the latter type of theories. It couples cellular-scale discrete agents with an averaged continuous theory based on the phase-field method. The model has shown significant potential predicting *in vivo* patterns of tumor-induced capillary growth. Besides its predictive capabilities, we feel this model is appealing for several reasons: (i) the model can easily accommodate cellular-scale kinetics into the discrete part; (ii) despite the complexity of the vasculature patterns, the continuous part is simply defined by a system of two partial differential equations on a fixed domain. This is due to the use of the phase-field method to describe the capillary patterns. The phase-field method is a mathematical theory introduced to solve interfacial problems. Originally developed for microstructure evolution [27, 28] and phase transition [29–31], it has been successfully applied to a number of physical phenomena such as infiltration [32], multicellular systems [33], or fluid vesicles [34]. Even more relevant to this article is the recent application of the phase-field method to modeling cancer growth [35, 36]. In opposition to the classical description of sharp interfaces, the phase-field model describes the interface between phases as diffuse. This permits avoiding the resolution of moving boundary problems, but requires solving a higher-order partial differential equation with diffuse interfaces evolving dynamically over the computational domain. In what follows, we present our methodology to treat these computational challenges.

1.4. Computer simulation of the tumor angiogenesis model

The main difficulties in the numerical simulation of the considered angiogenesis model are the discrete/continuous coupling and the efficient approximation of the higher-order partial differential equation of the continuous description. To undertake the coupling, we put the model into a coherent mathematical framework, so that the discrete components are embedded into a global functional description that can be easily coupled with the continuous equations.

The numerical approximation of the higher-order partial differential equation describing the vascular networks entails several difficulties, such as stiffness in space and time, resolution of diffuse interfaces that evolve dynamically, and discretization of higher-order differential operators. In the literature, we found that on simple geometries, it is common to use the finite difference method [37, 38] or spectral methods [39] to approximate higher-order derivatives. However, our goal is to undertake the discrete/continuous coupling by using a global functional description adequate for finite element methods, which are geometrically flexible. Variational formulations of higher-order equations require the use of functions, which are globally highly continuous. In particular, the fourth-order equation that we solve in this paper requires globally $\mathcal{C}^1$-continuous functions. Although significant progress has been made, see for example [40], the derivation of three-dimensional and geometrically flexible $\mathcal{C}^1$-continuous finite elements is to the best of our knowledge an open problem. Most existing approaches require the introduction of additional degrees of freedom or stabilization parameters, which has made that the vast majority of the finite element community continues to utilize mixed methods [41] that permit the use of $\mathcal{C}^0$-continuous elements. Alternative approaches outside the classical continuous finite element methods include, among others, the discontinuous Galerkin method [42], the continuous/discontinuous Galerkin method [43], or maximum entropy approximations [44–46]. Recently, Hughes *et al.* [47] developed a new technology, isogeometric analysis (IGA) [48–54], which deals perfectly with the problems of the phase-field models and, particularly, with the model proposed in [26]. The characteristics that make IGA suitable for our problems are higher-order accuracy, robustness [55], two-dimensional and three-dimensional geometric flexibility, compact support, and $\mathcal{C}^1$ continuity [56–58].
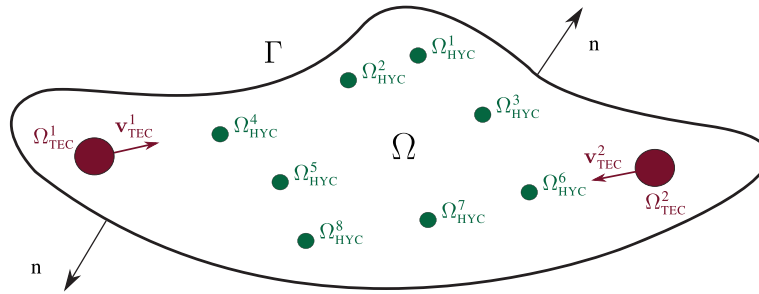
Figure 2. Two-dimensional representation of the different spatial domains involved in the model. The boundary Γ of the domain Ω has natural boundary conditions. The unit outward the boundary is denoted by **n**. In addition, there are two types of circular subdomains in Ω, namely Ω_{TEC}^i (red) that move with a velocity $\mathbf{v}_{\text{TEC}}^i$, where $i = 1, 2$, and Ω_{HYC}^j, $j = 1, \ldots, 8$, (green) with fixed positions. Ω simulates a tissue, Ω_{TEC} the tip endothelial cells, and Ω_{HYC} the hypoxic cells.

In this paper, we present a numerical method based on IGA that naturally couples the discrete cellular-scale kinetics with the continuous description of the macroscale. We develop a mathematical framework that permitted us to include the mobile discrete agents that represent cells, into the dynamics of the continuous variables. The latter combined with the high-order accuracy and the $\mathcal{C}^1$ continuity of IGA lead to highly efficient algorithms for solving the mathematical model. The accuracy and versatility of the method allowed us to perform several simulations that provide insight into the dynamics of the governing equations and the underlying biological process. It may be noted that, although the numerical examples presented in this paper are two dimensional, both the theory and the numerical algorithms can be easily extended to three-dimensional settings.

The rest of the paper is organized as follows: we describe the tumor angiogenesis model in Section 2 and propose a numerical method to solve it in Section 3. In Section 4, we show the time evolution of a numerical example, a parametric study of the model and several simulations under different initial conditions. We finalize with the conclusions in Section 5.

2. THE TUMOR ANGIOGENESIS MODEL

Our modeling strategy is based on the theory proposed by Travasso *et al.* in [26], which is a multi-scale, hybrid model that describes the vascular development caused by the tumor angiogenesis factor released by HYCs. The model accounts for multiple biological phenomena, such as the release of TAF by HYCs; the activation of quiescent endothelial cells, and their differentiation into SECs and TECs; and the capillary growth by chemotaxis. These biological processes are summarized in Figure 1, where we also show in light gray fonts some other phenomena not accounted for in the theory. In [26], the authors focus on the predictive capabilities of the model, showing that it reproduces *in vivo* patterns of newly formed vascular networks. Here, we emphasize the mathematical and algorithmic aspects of the numerical approximation of the theory. In this section, we put the model into a coherent mathematical and algorithmic framework. We understand the model as a staggering scheme that alternatively uses the continuous and discrete descriptions. Therefore, before introducing the fundamental equations of the model, we need to discretize the time interval of interest, namely $(0, T)$, into N sub-intervals $I_n = (t_n, t_{n+1})$, $n = 0, 1, \ldots, N - 1$, where $0 = t_0 < t_1 < \cdots < t_N = T$. We will use the notation $\Delta t_n = t_{n+1} - t_n$. To advance the variables of interest, namely the phase field describing the endothelial cells location (c) and the TAF concentration (f), we need to solve first a discrete, agent-based model and subsequently a continuous boundary value problem. The discrete and continuous problems are defined on different spatial domains that we introduce in what follows. For a pictorial description of the spatial domains involved in the model, the reader is referred to Figure 2.

2.1. The spatial domain of the continuous problem

Let $\Omega \subset \mathbb{R}^d$ be an open set, where $d = 2$ or 3, and let Γ be the boundary of the domain Ω. The boundary Γ is assumed to be sufficiently smooth (e.g., Lipschitz) and to have a well-defined unit outward normal denoted by $\mathbf{n}$. The set Ω represents a portion of tissue that remains fixed over the time interval $(0, T)$ and is associated to the continuous part of the model. In Ω, we will define the fields $c : \Omega \times (0, T) \mapsto [-1, 1]$ and $f : \Omega \times (0, T) \mapsto [0, f_{\mathrm{HYC}}]$, which represent, respectively, the phase field describing the endothelial cells location and the TAF concentration, where f_{HYC} is a positive constant.

2.2. The spatial domain of the discrete model

The discrete component of the model takes place on two subsets of Ω that may vary from one time step to the next. We call these subdomains the HYC subdomain and the TEC subdomain.

2.2.1. The hypoxic cell subdomain.
This subdomain is associated to HYC locations, where the TAFs are released. At the initial time stage, t_0, we define this set as $\Omega_{\mathrm{HYC}}(t_0) = \bigcup_{i=1}^{N_{\mathrm{HYC}}} \Omega_{\mathrm{HYC}}^i(t_0)$, where each of the $\Omega_{\mathrm{HYC}}^i(t_0)$ is a circular-shaped (spherical-shaped if $d = 3$) subset of Ω with radius R_{HYC} and center $\mathbf{x}_{\mathrm{HYC}}^i$. This can be considered as an initial condition, which determines the location of the HYCs that release TAF, triggering the growth of new capillaries. This set may vary from one time step to the next, because some TAF sources may become inactive and stop releasing TAF. In particular, at each time step, the set $\Omega_{\mathrm{HYC}}(t_{n+1})$ is obtained from $\Omega_{\mathrm{HYC}}(t_n)$ using biologically motivated deterministic conditions to be defined in Section 2.4. If at the time stage t_n a particular subdomain indexed by j meets those conditions, then $\Omega_{\mathrm{HYC}}^j(t_{n+1}) = \Omega_{\mathrm{HYC}}^j(t_n)$. If those conditions fail to be satisfied, then $\Omega_{\mathrm{HYC}}^j(t_{n+1}) = \emptyset$.

2.2.2. The tip endothelial cell subdomain.
This subdomain is associated to TECs, which are mobile discrete agents in the model. At the initial time stage t_0, there are no active TECs, and, thus $\Omega_{\mathrm{TEC}}(t_0) = \emptyset$. As time evolves, some TECs will become activated, leading at the stage t_n, to a set $\Omega_{\mathrm{TEC}}(t_n) = \bigcup_{i=1}^{N_{\mathrm{TEC}}(t_n)} \Omega_{\mathrm{TEC}}^i(t_n)$, where each of the $\Omega_{\mathrm{TEC}}^i(t_n)$ is a circular-shaped (spherical-shaped if $d = 3$) subset of Ω with radius R_{TEC} and center $\mathbf{x}_{\mathrm{TEC}}^i$. Note that the number of subdomains composing Ω_{TEC} may vary from one time step to the next, because new subdomains are created when new TECs become active. The biological conditions under which a new subdomain is created will be defined in Section 2.4. Once a TEC subdomain is created, it needs to satisfy some conditions (also to be defined in Section 2.4) to remain active. If an existing subdomain fails to satisfy those conditions at the time stage t_n, it will become the empty set at stage t_{n+1}. Each of the existing subdomains that still satisfy the conditions at the stage t_n gives rise to a new, but different, subdomain at the time stage t_{n+1}. Let us assume that $\Omega_{\mathrm{TEC}}^k(t_n)$ is one of these subdomains. Its corresponding subdomain at time t_{n+1} is obtained by applying an affine transformation to $\Omega_{\mathrm{TEC}}^k(t_n)$. The affine transformation, namely φ_n^k, is defined by

$$\varphi_n^k(\mathbf{x}) = \mathbf{x} + \Delta t_n \mathbf{v}_{\mathrm{TEC}}^k \tag{1}$$

and the new subdomain is defined as $\Omega_{\mathrm{TEC}}^k(t_{n+1}) = \varphi_n^k\left(\Omega_{\mathrm{TEC}}^k(t_n)\right)$. In Equation (1), $\mathbf{v}_{\mathrm{TEC}}^k$ represents the velocity of the TEC and is defined by

$$\mathbf{v}_{\mathrm{TEC}}^k = \chi \nabla f(\mathbf{x}_{\mathrm{TEC}}^k) \mathcal{L}\left(\|\nabla f(\mathbf{x}_{\mathrm{TEC}}^k)\|\right) \tag{2}$$

where χ is a chemotactic constant, $\mathcal{L}$ is a limiting function to be defined in Section 2.4, and the operator $\|\cdot\|$ denotes the Euclidean norm of a vector. Note that Equations (1) and (2) treat the TECs as discrete mobile agents, assigning them an individual velocity.

2.3. The coupled discrete/continuous model

Here, we present the algorithmic rules to advance the fields of interest from one time step, say t_n, to the next. Given $c(\cdot, t_n)$, $f(\cdot, t_n)$, $\{\Omega^i_{\mathrm{HYC}}(t_n)\}_{i=1,N_{\mathrm{HYC}}}$, and $\{\Omega^i_{\mathrm{TEC}}(t_n)\}_{i=1,N_{\mathrm{TEC}}(t_n)}$, proceed as follows:

1. Find $\{\Omega^i_{\mathrm{HYC}}(t_{n+1})\}_{i=1,N_{\mathrm{HYC}}}$ and $\{\Omega^i_{\mathrm{TEC}}(t_{n+1})\}_{i=1,N_{\mathrm{TEC}}(t_{n+1})}$ following the steps indicated in Sections 2.2.1 and 2.2.2 and the conditions defined in Section 2.4.
2. Set $f = f_{\mathrm{HYC}}$ in $\Omega_{\mathrm{HYC}}(t_{n+1})$, overwriting the values of $f(\cdot, t_n)$ in $\Omega_{\mathrm{HYC}}(t_{n+1})$. Call the resulting field $\widetilde{f}(\cdot, t_n)$.
3. Set

$$c = c^i_{\mathrm{TEC}} = \frac{\mathcal{B}_{\mathrm{p}}\left(f\left(\mathbf{x}^i_{\mathrm{TEC}}\right)\right) \pi R_{\mathrm{TEC}}}{2\|\mathbf{v}^i_{\mathrm{TEC}}\|} \tag{3}$$

in $\Omega^i_{\mathrm{TEC}}(t_{n+1})$ for all $i = 1, \ldots, N_{\mathrm{TEC}}(t_{n+1})$, overwriting the values of $c(\cdot, t_n)$ in $\Omega_{\mathrm{HYC}}(t_{n+1})$ for all $i = 1, \ldots, N_{\mathrm{TEC}}(t_{n+1})$. Call the resulting field $\widetilde{c}(\cdot, t_n)$.
4. Solve the boundary value problem

$$\frac{\partial f}{\partial t} = \nabla \cdot (D \nabla f) - B_{\mathrm{u}} f c \mathcal{H}(c) \qquad \text{in} \quad \Omega \times (t_n, t_{n+1}) \tag{4}$$

$$\frac{\partial c}{\partial t} = \nabla \cdot \left(M \nabla \left(\mu_{\mathrm{c}} - \lambda^2 \Delta c\right)\right) + \mathcal{B}_{\mathrm{p}}(f) c \mathcal{H}(c) \qquad \text{in} \quad \Omega \times (t_n, t_{n+1}) \tag{5}$$

$$D \nabla f \cdot \mathbf{n} = 0 \qquad \text{on} \quad \Gamma \times (t_n, t_{n+1}) \tag{6}$$

$$M \nabla \left(\mu_{\mathrm{c}} - \lambda^2 \Delta c\right) \cdot \mathbf{n} = 0 \qquad \text{on} \quad \Gamma \times (t_n, t_{n+1}) \tag{7}$$

$$M \lambda^2 \Delta c = 0 \qquad \text{on} \quad \Gamma \times (t_n, t_{n+1}) \tag{8}$$

$$f(\mathbf{x}, t_n) = \widetilde{f}(\mathbf{x}, t_n) \qquad \text{in} \quad \Omega \tag{9}$$

$$c(\mathbf{x}, t_n) = \widetilde{c}(\mathbf{x}, t_n) \qquad \text{in} \quad \Omega \tag{10}$$

The notation in the boundary value problem is as follows: D is the diffusion constant; B_{u} is the uptake rate constant; $\mathcal{H}(\cdot)$ is the Heaviside function; M is the constant mobility; μ_{c} is the chemical potential; λ is a positive constant proportional to the width of the capillaries wall; and $\mathcal{B}_{\mathrm{p}}(\cdot)$ is the proliferative rate function. In what follows, we describe in detail all the functions and algorithmic rules involved in the theory.

2.4. The discrete component

The discrete, agent-based component of the model includes the production of angiogenic factor by the HYCs, the deactivation of the HYCs, and the activation, migration, and deactivation of the TECs.

2.4.1. Hypoxic cells.
The TAF is produced by randomly distributed HYCs with fixed positions denoted by $\mathbf{x}^i_{\mathrm{HYC}}$. It is assumed that the HYCs create a subdomain Ω^i_{HYC} around them in which the value of f remains constant and equal to f_{HYC} while the HYC is active. The HYCs are only deactivated, ceasing their production, when a capillary, considered here as all those points in which $c \geqslant c_{\mathrm{act}}$, is closer than a distance δ_{nox}. This distance represents the diffusion length of the nutrients and oxygen from the blood vessels.

2.4.2. Activation of tip endothelial cells.
When the TAF reaches a capillary, a new TEC is activated if the following conditions are met in a point $\mathbf{x}^* \in \Omega$:

1. $c \geqslant c_{\mathrm{act}}$,
2. $f \geqslant f_{\mathrm{act}}$,
3. $G \geqslant G_{\mathrm{act}}$, and
4. $\|\mathbf{x}^* - \mathbf{x}^j_{\mathrm{TEC}}\| \geqslant \delta_4, \forall j = 1, \ldots, N_{\mathrm{TEC}}(t_n)$.

Condition 1 restricts the candidate points to TECs to those satisfying $c \geqslant c_{\text{act}}$, that is, those inside a capillary. The following two are lower limit conditions: the value of the factor f and the modulus of its gradient $G = \|\nabla f\|$ must be greater than certain thresholds defined by $f \geqslant f_{\text{act}}$ and $G \geqslant G_{\text{act}}$. Finally, condition 4 accounts for the differentiation phenomena described earlier driven by the Dll-4 ligand and the Notch receptor. In the model, no point can be activated as the position of the new TEC if there is another closer than a certain distance δ_4. This distance represents the diffusion length of the ligand Dll-4.

If the four conditions are met in $\mathbf{x}^*$, then a new subdomain is created. Let us assign the index l to the new subdomain $\Omega^l_{\text{TEC}}(t_{n+1})$, which is centered at $\mathbf{x}^* = \mathbf{x}^l_{\text{TEC}}$ and defined as

$$\Omega^l_{\text{TEC}}(t_{n+1}) = \left\{ \mathbf{x} \in \Omega \,\middle|\, \|\mathbf{x} - \mathbf{x}^l_{\text{TEC}}\| \leqslant R_{\text{TEC}} \right\} \tag{11}$$

If there are two or more points that satisfy the conditions, only one TEC is created per time step. Inside the subdomain $\Omega^l_{\text{TEC}}(t_{n+1})$, the value of the concentration of endothelial cells is described by Equation (3), thus merging the discrete component with the continuous description. This value is the ratio of the material produced in the subdomain by proliferation and the area swept in the movement of the TEC, assuming that the problem is posed on a two-dimensional domain.

2.4.3. Migration of tip endothelial cells. The subdomains $\left\{ \Omega^j_{\text{TEC}} \right\}_{j=1,\ldots,N_{\text{TEC}}(t_n)}$ are updated using Equation (1), which translates them into the direction of the gradient of angiogenic factor with a modulus proportional to this gradient through χ. In addition, the modulus of the velocity is affected by a function given by

$$\mathcal{L}(\|\nabla f\|) = 1 + \left(\frac{G_{\text{M}}}{\|\nabla f\|} - 1 \right) \mathcal{H}(\|\nabla f\| - G_{\text{M}}) \tag{12}$$

where G_{M} is a constant. This function maintains the modulus of the velocity under a threshold, namely $v_{\text{TEC,max}} = \chi G_{\text{M}}$. Both the function and its effect on the velocity are represented in Figure 3.

2.4.4. Deactivation of tip endothelial cells. The deactivation of the TECs is accomplished through two conditions. Whenever the value of the TAF or its gradient is less than their activation thresholds, f_{act} and G_{act}, respectively, the corresponding TEC is deactivated, vanishing its associated subdomain.

2.5. The boundary value problem

The boundary value problems (4)–(10) determine the continuous part of the model. The TAF diffuses throughout the domain Ω according to Equation (4) and is consumed by the endothelial cells at
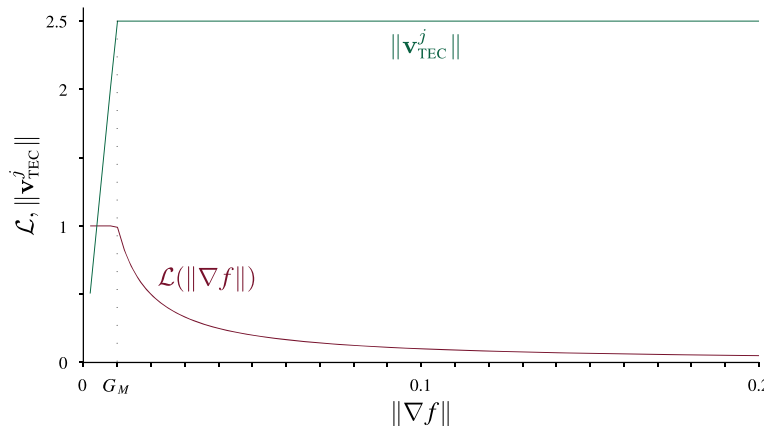

Figure 3. Limiting function, $\mathcal{L}(\cdot)$, for the velocity of the tip endothelial cells plotted in red and velocity modulus, $\|\mathbf{v}^j_{\text{TEC}}\|$, plotted in green. For this graph, $\chi = 250$ and $G_{\text{M}} = 0.03$.

a rate of B_u, as modeled by the reactive term in the equation. Free flux conditions are imposed on the boundary Γ through Equation (6). The initial conditions for the TAF at each time stage are described by Equation (9). The dynamics of the endothelial cells are modeled by a phase-field Equation (5), where c is the order parameter of the concentration of endothelial cells. If we assume that the reactive term $\mathcal{B}_p(f)c\mathcal{H}(c)$ is small, the evolution of c is such that it tends to adopt the configuration of minimum energy given by the energy functional:

$$\mathcal{E}(c) = \int_\Omega (\Psi_c + \Psi_s)\, d\mathbf{x} \tag{13}$$

where Ψ_c is the chemical free energy and Ψ_s is the surface free energy. The chemical free energy, given by

$$\Psi_c = -\frac{c^2}{2} + \frac{c^4}{4} \tag{14}$$

is a double-well, non-convex function with two local minima, each one representing a phase, as shown on the left-hand side of Figure 4. One of the minima is at $c = 1$, where the concentration of endothelial cells is maximum, and the other at $c = -1$, where there are no endothelial cells, but only host tissue cells. The local maximum in $c = 0$ corresponds to the capillary walls. The energy term Ψ_c leads to the separation of the phases. The chemical potential μ_c is given by $\mu_c = \Psi_c' = -c + c^3$, where Ψ_c' is the derivative of the chemical free energy with respect to c. The surface free energy is defined as

$$\Psi_s = \frac{1}{2}\lambda^2\|\nabla c\|^2 \tag{15}$$

where λ is a length scale of the model. The surface term endows the capillary walls with an energy, penalizing the appearance of new sprouts. Equation (5) also involves a reactive term that makes the theory non-conservative [59]. This term is introduced to model the proliferation of endothelial cells in the presence of angiogenic factor. The proliferative rate function $\mathcal{B}_p(f)$, present in the reactive term, and given by

$$\mathcal{B}_p(f) = \begin{cases} B_p f & \text{if } f < f_p \\ B_p f_p & \text{if } f \geqslant f_p \end{cases} \tag{16}$$

increases with the value of the factor until a threshold f_p. Above f_p, the proliferation remains constant. The function is plotted on the right-hand side of Figure 4. For the phase-field equation, we also apply free flux boundary conditions on Γ, described by Equations (7) and (8). At each time step, the initial condition for the phase field is defined by (10).

2.6. Parameters

Many of the parameters that characterize the equations of the model were obtained by Travasso *et al.* from observed values *in vivo* (see references in [26]). On the contrary, those related with the
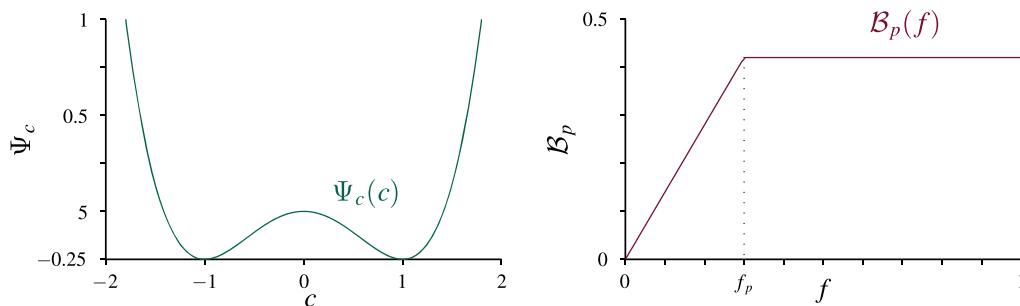

Figure 4. Plot of the energy functional (left) that leads to phase separation and plot of the proliferation function (right) that controls the proliferation of the endothelial cells.

Table I. *In vivo* and *in silico* values of the parameters of the model.

Parameter	Symbol	*In vivo* value	*In silico* value
TEC radius	R_{TEC}	5 µm	4
HYC radius	R_{HYC}	5 µm	4
Oxygen diffusion length	δ_{nox}	25 µm	20
Dll-4 diffusion length	δ_4	20 µm	16
Interface width	λ	1.25 µm	1
Diffusion constant	D	10^{-13} m^2 s^{-1}	100
Constant mobility	M	10^{-15} m^2 s^{-1}	1
Uptake rate constant	B_{u}	0.004 s^{-1}	6.25
Proliferative rate	B_{p}		1.401
Chemotactic constant	χ		242.67
TAF production	f_{HYC}		1
TAF condition for highest proliferation	f_{p}		0.3
Order parameter condition for activation/deactivation	c_{act}		0.9
TAF condition for activation/deactivation	f_{act}		0.055
TAF gradient condition for activation/deactivation	G_{act}		0.01
TAF gradient for highest velocity	G_{M}		0.03

The *in vivo* parameters were obtained from experiments detailed in the references of [26].

TAF quantity and the condition of the order parameter for TEC activation (c_{act}) are estimated for the simulation (we note that, in this context, the validation/calibration methodology for parameters presented in [60] may be relevant). As the equations are written in dimensionless form, it is necessary to obtain the corresponding dimensionless parameters, referred to as the *in silico* value of the parameters, for those that come from *in vivo* observation. The length and time scales $L_0 = 1.25$ µm and $T_0 = 1560$ s allow to retrieve physical values from the simulation results. Table I presents all the parameters of the model, including the *in vivo* and *in silico* values.

3. NUMERICAL METHOD

In this section, we proposed a numerical method for solving the equations of the mathematical model. We consider separately the discrete component and the boundary value problem (4)–(10). We explain first the numerical method for the discrete component in Section 3.1, where we describe how the discrete rules are considered and how the discrete component is merged with the continuous equations. Section 3.2 describes the algorithms utilized to discretize the continuous problem. We start by deriving a weak form, following with the spatial and time discretization using the Galerkin method and the generalized-α algorithm, respectively. The resulting non-linear system is solved using a predictor multi-corrector algorithm based on the Newton–Raphson method. Finally, we present a time-step size selection algorithm. For the reader's convenience, we present a flowchart of the numerical method in Figure 5.

3.1. The discrete component

The numerical method for the discrete module of the theory is composed of two parts, namely the update of the spatial domains Ω_{HYC} and Ω_{TEC}, and the algorithm to overwrite the values of the fields f and c on Ω_{HYC} and Ω_{TEC}, respectively.

3.1.1. Update of the spatial domains of the discrete component.
We define a sufficiently fine uniform grid of sample points (typically, twice as fine as that used for the continuous boundary value problem), where we calculate the values of the TAF, its gradient, and the order parameter. With these evaluations, we are able to determine whether the discrete rules for the activation and deactivation of the TECs are satisfied. In addition, we are provided with the value of the order parameter in those points that are closer than a distance δ_{nox} from the center of the subdomains $\{\Omega_{\text{HYC}}^i\}_{i=1,\ldots,N_{\text{HYC}}}$ that permit us to deactivate the HYC according to the discrete rules. Finally, we evaluate the TAF, its
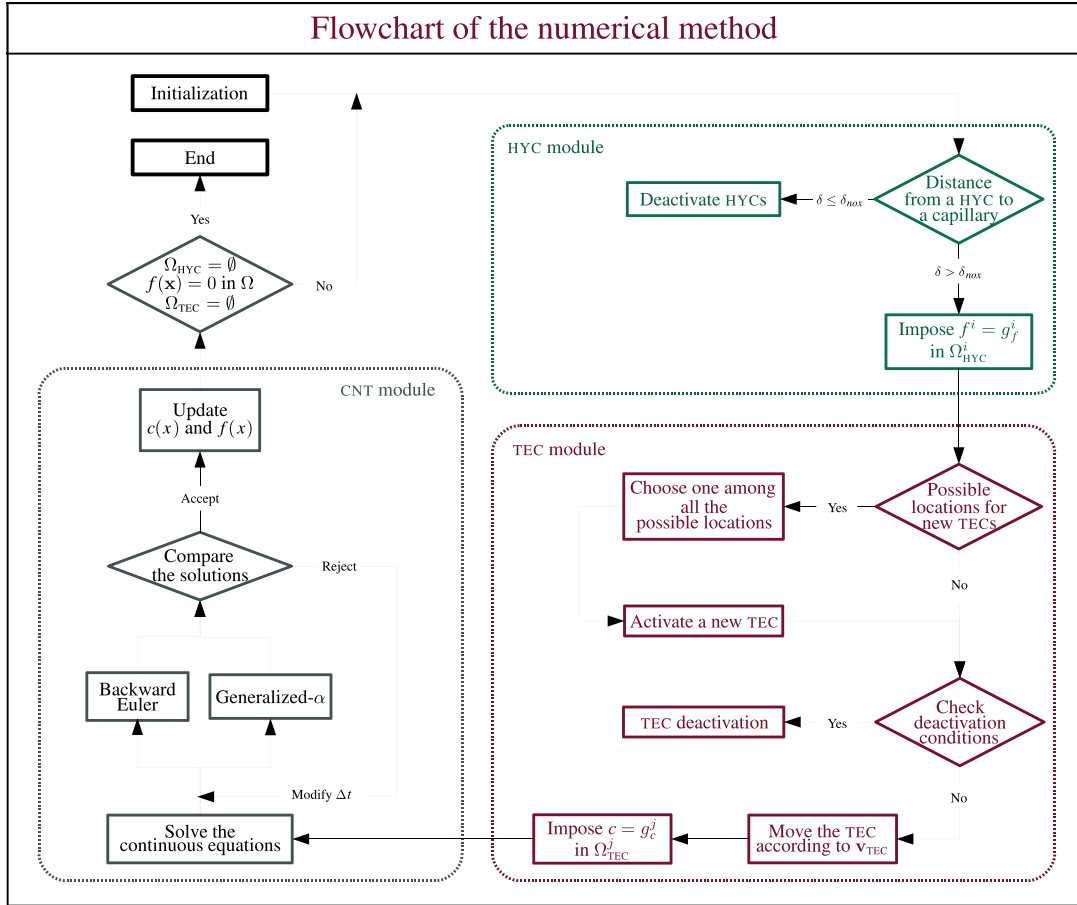
Figure 5. The numerical method starts by an initialization. Then two modules that deal with the discrete component come into play: the hypoxic cell module (HYC) first (in green) and the tip endothelial cell module (TEC) afterward (in red). The first action performed in both the HYC and TEC modules is the implementation of the discrete rules defined in Section 2.4, namely the deactivation of the HYCs near a capillary and the activation/deactivation and the movement of the TECs. At the end of the modules, the values of f and c are modified in Ω_{HYC} and Ω_{TEC}, respectively. Finally, in the module for the continuous equations (CNT), plotted in gray, the boundary value problem is solved. The resolution of the equations uses the method proposed in Section 3.2, including the adaptive time-step Algorithm 1. This process is repeated until there are no HYCs, neither TECs, and the TAF is consumed.

gradient, and the order parameter in the center of the subdomains $\{\Omega_{\text{TEC}}^i\}_{i=1,\dots,N_{\text{TEC}}(t_n)}$ to calculate the corresponding imposed order parameter c_{TEC}^j and velocity $\mathbf{v}_{\text{TEC}}^j$ necessary to move the subdomains using Equation (1).

3.1.2. Impose the constraints on the fields $c^h(\mathbf{x}, t_n)$ and $f^h(\mathbf{x}, t_n)$. As we will use IGA to solve the boundary value problems (4)–(10), the phase field and the TAF field will be elements of a finite dimensional space. This is why we use the notation $c^h(\mathbf{x}, t_n)$ and $f^h(\mathbf{x}, t_n)$ with the superscript h. We have to impose f_{HYC} in $\{\Omega_{\text{HYC}}^i\}_{i=1,\dots,N_{\text{HYC}}}$ and c_{TEC}^j in Ω_{TEC}^j, $\forall j = 1, \dots N_{\text{TEC}}(t_n)$, according to Equation (3). Let us illustrate how we overwrite the value of $c^h(\mathbf{x}, t_n)$ on a given subdomain $\Omega_{\text{TEC}}^j(t_n)$, where j is a fixed index that takes one of its admissible values, namely $1, \dots, N_{\text{TEC}}(t_n)$. Let us define the template function $g_c^j : \Omega \mapsto [-1, 1]$ as

$$g_c^j(\mathbf{x}) = \left(\frac{c_{\text{TEC}}^j - 1}{2} \right) - \left(\frac{c_{\text{TEC}}^j + 1}{2} \right) \tanh \left(\frac{\|\mathbf{x} - \mathbf{x}_{\text{TEC}}^j\| - R_{\text{TEC}}}{2\epsilon} \right) \tag{17}$$
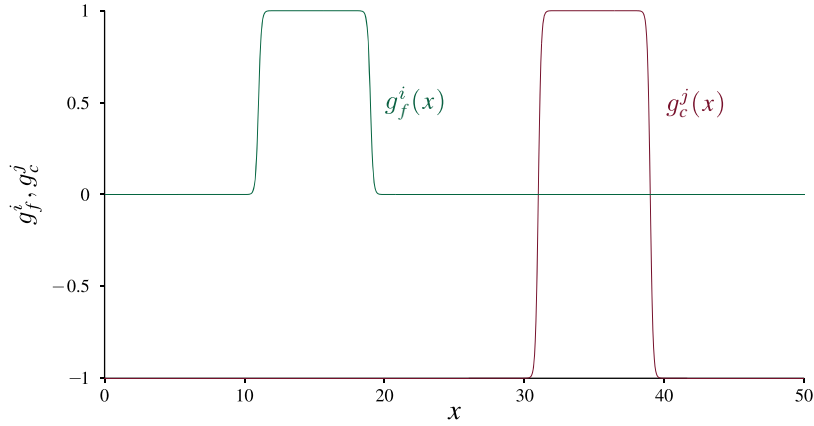
Figure 6. One-dimensional examples of the template functions used to merge the discrete component with the continuous variables. We plot $g^i_f(x)$ in green and $g^j_c(x)$ in red, where $\Omega^i_{\text{HYC}}(t_n) = (10, 20)$, $\Omega^j_{\text{TEC}}(t_n) = (30, 40)$, and $c^j_{\text{TEC}} = 1$.

where $\epsilon = 0.1$. Note that g^j_c is a multidimensional generalization of an exact one-dimensional solution to the Cahn–Hilliard equation on an infinite domain. Thus, we overwrite the value of $c^h(\mathbf{x}, t_n)$, using a template function as close as possible to the fundamental solution of the partial differential Equation (5). Figure 6 presents a one-dimensional illustration of g^j_c in which $\Omega^j_{\text{TEC}}(t_n) = (30, 40)$. Taking into account all of this, our goal is to find

$$\widetilde{c}^j(\mathbf{x}, t_n) = \begin{cases} g^j_c(\mathbf{x}) & \text{if } \mathbf{x} \in \Omega^j_{\text{TEC}} \\ c(\mathbf{x}, t_n) & \text{otherwise} \end{cases} \tag{18}$$

To undertake the coupling between the discrete and continuous parts of the algorithm, we need to find an approximation of $\widetilde{c}^j(\mathbf{x}, t_n)$ that lives in the finite dimensional space. Let us call Π the L^2 projection operator associated to the discrete space. We define $\widetilde{c}^{j,h}(\mathbf{x}, t_n) = \Pi\left(\widetilde{c}^j(\mathbf{x}, t_n)\right)$. This process can be repeated for all relevant j to obtain the overwritten field $\widetilde{c}^h(\mathbf{x}, t_n)$.

We proceed analogously to impose the constraints on the field $f^h(\mathbf{x}, t_n)$. This case is somewhat simpler because the imposed value f_{HYC} will always be greater than the value of the field $f^h(\mathbf{x}, t_n)$ because of the maximum principle satisfied by Equation (4). Let us illustrate the process by imposing the restriction on $\Omega^i_{\text{HYC}}(t_n)$. We define the template function $g^i_f : \Omega \mapsto [0, f_{\text{HYC}}]$ as

$$g^i_f(\mathbf{x}) = \frac{1}{2} - \frac{1}{2} \tanh\left(\frac{\|\mathbf{x} - \mathbf{x}^i_{\text{HYC}}\| - R_{\text{HYC}}}{2\epsilon}\right) \tag{19}$$

Figure 6 shows a one-dimensional illustration of the template function. As g^i_f will be greater than $f^h(\mathbf{x}, t_n)$ in $\Omega^i_{\text{HYC}}(t_n)$, we can define $\widetilde{f}^i(\mathbf{x}, t_n)$ as

$$\widetilde{f}^i(\mathbf{x}, t_n) = \max\left(f^h(\mathbf{x}, t_n), g^i_f(\mathbf{x})\right) \tag{20}$$

The process is finalized projecting $\widetilde{f}^i$ onto the discrete space as $\widetilde{f}^{i,h}(\mathbf{x}, t_n) = \Pi\left(\widetilde{f}^i(\mathbf{x}, t_n)\right)$ and repeating for all relevant i.

Remark

1. Only when the value of c^j_{TEC} is greater than $c\left(\mathbf{x}^j_{\text{TEC}}, t_n\right)$, Equation (18) reduces to

$$\widetilde{c}^j(\mathbf{x}, t_n) = \max\left(c^h(\mathbf{x}, t_n), g^j_c(\mathbf{x})\right) \tag{21}$$

However, in the opposite case, $c_{\mathrm{TEC}}^j \leqslant c\left(\mathbf{x}_{\mathrm{TEC}}^j, t_n\right)$, we also use the latter equation. We have verified that using this simplification rather than Equation (18) does not lead to significant changes in the solutions.

3.2. The continuous equations

We begin by considering a weak form of Equations (4) and (5). Let $\mathcal{V}$ denote the trial and weighting function spaces, which are assumed to be identical. The space $\mathcal{V}$ is a subset of $\mathcal{H}^2$, the Sobolev space of square integrable functions with square integrable first and second derivatives. The weak form of the problem is obtained by multiplying Equations (4) and (5) with smooth functions, integrating over the domain, and applying integration by parts repeatedly under the assumption of free flux boundary conditions. The problem may be stated as follows: find $f, c \in \mathcal{V}$ such that $\forall w, q \in \mathcal{V}$:

$$
\left.\begin{aligned}
\left(w, \frac{\partial f}{\partial t}\right)_\Omega + (\nabla w, D\nabla f)_\Omega + (w, B_{\mathrm{u}} fc\mathcal{H}(c))_\Omega &= 0 \\
\left(q, \frac{\partial c}{\partial t}\right)_\Omega + (\nabla q, M\nabla\mu_{\mathrm{c}})_\Omega + \left(\Delta q, M\lambda^2\Delta c\right)_\Omega - (q, \mathcal{B}_{\mathrm{p}}(f)c\mathcal{H}(c))_\Omega &= 0
\end{aligned}\right\}
\tag{22}
$$

where $(\cdot, \cdot)_\Omega$ is the L^2 inner product with respect to the domain Ω. We make use of the Galerkin method to obtain the spatial discretization of the previous weak formulation. We approximate (22) by the following variational problem over the finite dimensional spaces: find $f^h, c^h \in \mathcal{V}^h \subset \mathcal{V}$ such that $\forall w^h, q^h \in \mathcal{V}^h \subset \mathcal{V}$:

$$
\left.\begin{aligned}
\left(w^h, \frac{\partial f^h}{\partial t}\right)_\Omega + \left(\nabla w^h, D\nabla f^h\right)_\Omega + \left(w^h, B_{\mathrm{u}} f^h c^h \mathcal{H}\left(c^h\right)\right)_\Omega &= 0 \\
\left(q^h, \frac{\partial c^h}{\partial t}\right)_\Omega + \left(\nabla q^h, M\nabla\mu\left(c^h\right)\right)_\Omega + \left(\Delta q^h, M\lambda^2\Delta c^h\right)_\Omega - \left(q^h, \mathcal{B}_{\mathrm{p}}\left(f^h\right)c^h\mathcal{H}\left(c^h\right)\right)_\Omega &= 0
\end{aligned}\right\}
\tag{23}
$$

Here, f^h is defined as

$$
f^h(\mathbf{x}, t) = \sum_{A=1}^{n_b} f_A(t) N_A(\mathbf{x})
\tag{24}
$$

where n_b is the dimension of the discrete space $\mathcal{V}^h$ and f_A are the so-called control variables, which act as coefficients of the basis functions N_A. The functions c^h, w^h, and q^h, which also live in the space $\mathcal{V}^h$, are defined analogously. As we will use a conforming discretization, the relation $\mathcal{V}^h \subset \mathcal{V}$ holds, and the discrete functions are required to be in $\mathcal{H}^2$. This condition is satisfied by the globally $\mathcal{C}^1$-continuous basis functions that we consider in this paper, by means of IGA. The most widely used basis functions in IGA are non-uniform rational B-splines that reduce to B-splines, in a two-dimensional, square geometry. These are the functions that we utilize in this paper.

We integrate in time using the generalized-α method. The generalized-α method is a second-order accurate, unconditionally A-stable method with controllable high-frequency dissipation that can be easily implemented within an adaptive time-step framework. All these features make it a good choice for the problem addressed in this paper. We use the notation $\dot{f}_n^h, f_n^h, \dot{c}_n^h, c_n^h$ for the fully discrete solutions of the TAF time derivative, the TAF, the phase-field time derivative, and the phase field, respectively.

The problem can be stated as follows: given $\dot{f}_n^h, f_n^h, \dot{c}_n^h, c_n^h$ and $\Delta t_n = t_{n+1} - t_n$, find $\dot{f}_{n+1}^h, f_{n+1}^h, \dot{c}_{n+1}^h, c_{n+1}^h$, such that

$$
\left.\begin{aligned}
\left(w^h, \dot{f}_{n+\alpha_m}^h\right)_\Omega + \left(\nabla w^h, D\nabla f_{n+\alpha_f}^h\right)_\Omega + \left(w^h, B_{\mathrm{u}} f_{n+\alpha_f}^h c_{n+\alpha_f}^h \mathcal{H}\left(c_{n+\alpha_f}^h\right)\right)_\Omega &= 0 \\
\left(q^h, \dot{c}_{n+\alpha_m}^h\right)_\Omega + \left(\nabla q^h, M\nabla\mu\left(c_{n+\alpha_f}^h\right)\right)_\Omega + \left(\Delta q^h, M\lambda^2\Delta c_{n+\alpha_f}^h\right)_\Omega & \\
- \left(q^h, \mathcal{B}_{\mathrm{p}}\left(f_{n+\alpha_f}^h\right)c_{n+\alpha_f}^h\mathcal{H}\left(c_{n+\alpha_f}^h\right)\right)_\Omega &= 0
\end{aligned}\right\}
\tag{25}
$$

where

$$f_{n+1}^h = f_n^h + \Delta t_n \dot{f}_n^h + \gamma \Delta t_n \left(\dot{f}_{n+1}^h - \dot{f}_n^h \right), \qquad c_{n+1}^h = c_n^h + \Delta t_n \dot{c}_n^h + \gamma \Delta t_n \left(\dot{c}_{n+1}^h - \dot{c}_n^h \right),$$

$$\dot{f}_{n+\alpha_m}^h = \dot{f}_n^h + \alpha_m \left(\dot{f}_{n+1}^h - \dot{f}_n^h \right), \qquad \dot{c}_{n+\alpha_m}^h = \dot{c}_n^h + \alpha_m \left(\dot{c}_{n+1}^h - \dot{c}_n^h \right),$$

$$f_{n+\alpha_f}^h = f_n^h + \alpha_f \left(f_{n+1}^h - f_n^h \right), \qquad c_{n+\alpha_f}^h = c_n^h + \alpha_f \left(c_{n+1}^h - c_n^h \right),$$

$$\gamma = \frac{1}{2} + \alpha_m - \alpha_f, \qquad \alpha_m = \frac{1}{2} \left(\frac{3 - \rho_\infty}{1 + \rho_\infty} \right), \qquad \alpha_f = \frac{1}{1 + \rho_\infty}$$

and ρ_∞ is the spectral radius of the amplification of the matrix as $\Delta t \to \infty$. We obtain second-order accuracy if $\gamma = \frac{1}{2} + \alpha_m - \alpha_f$ is satisfied and unconditional stability (for a linear problem) provided that $\alpha_m \geqslant \alpha_f \geqslant \frac{1}{2}$.

Now, let $\dot{\mathbf{F}}^n$, $\mathbf{F}^n$, $\dot{\mathbf{C}}^n$, and $\mathbf{C}^n$ be the vector of degrees of freedom of $\dot{f}_n^h$, f_n^h, $\dot{c}_n^h$, and c_n^h, respectively, and let $\mathbf{S}^n = \{\mathbf{F}^n, \mathbf{C}^n\}^{\mathrm{T}}$ be a vector of all the degrees of freedom. The time-stepping scheme may be implemented as follows: given $\dot{\mathbf{S}}^n$, $\mathbf{S}^n$, and Δt_n, find $\dot{\mathbf{S}}^{n+1}$ and $\mathbf{S}^{n+1}$ such that $\mathbf{R} = 0$, where

$$\mathbf{R} = \left\{ \begin{array}{c} R_A^f \\ R_A^c \end{array} \right\} \tag{26}$$

$$R_A^f = \left(N_A, \dot{f}_{n+\alpha_m}^h \right)_\Omega + \left(\nabla N_A, D \nabla f_{n+\alpha_f}^h \right)_\Omega + \left(N_A, B_{\mathrm{u}} f_{n+\alpha_f}^h c_{n+\alpha_f}^h \mathcal{H} \left(c_{n+\alpha_f}^h \right) \right)_\Omega \tag{27}$$

$$R_A^c = \left(N_A, \dot{c}_{n+\alpha_m}^h \right)_\Omega + \left(\nabla N_A, M \nabla \mu \left(c_{n+\alpha_f}^h \right) \right)_\Omega + \left(\Delta N_A, M \lambda^2 \Delta c_{n+\alpha_f}^h \right)_\Omega \tag{28}$$

$$- \left(N_A, \mathcal{B}_{\mathrm{p}} \left(f_{n+\alpha_f}^h \right) c_{n+\alpha_f}^h \mathcal{H} \left(c_{n+\alpha_f}^h \right) \right)_\Omega \tag{29}$$

Equating the residual to zero, we define a non-linear system of algebraic equations. We use the Newton–Raphson method to solve the system, which leads to a two-stage predictor–corrector algorithm:

1. *Predictor stage*: Set

$$\dot{\mathbf{S}}^{n+1,(0)} = \frac{\gamma - 1}{\gamma} \dot{\mathbf{S}}^n \tag{30}$$

$$\mathbf{S}^{n+1,(0)} = \mathbf{S}^n \tag{31}$$

2. *Multi-corrector stage*: Repeat the following steps for $i = 1, 2, \ldots, i_{\max}$ or until $\|\mathbf{R}_f^{n+1,(i)}\|/\|\mathbf{R}_f^{n+1,(0)}\| \leqslant \Upsilon_{\text{N-R}}$ and $\|\mathbf{R}_c^{n+1,(i)}\|/\|\mathbf{R}_c^{n+1,(0)}\| \leqslant \Upsilon_{\text{N-R}}$, where $\Upsilon_{\text{N-R}}$ is a given tolerance.

   (a) Evaluate the iterations at the α-levels

$$\dot{\mathbf{S}}^{n+\alpha_m,(i)} = \dot{\mathbf{S}}^n + \alpha_m \left(\dot{\mathbf{S}}^{n+1,(i-1)} - \dot{\mathbf{S}}^n \right) \tag{32}$$

$$\mathbf{S}^{n+\alpha_f,(i)} = \mathbf{S}^n + \alpha_f \left(\mathbf{S}^{n+1,(i-1)} - \mathbf{S}^n \right) \tag{33}$$

   (b) Assemble the residual vector and tangent matrix

$$\mathbf{R}^{n+1,(i)}; \qquad \mathbf{K}^{n+1,(i)} = \nabla_{\dot{\mathbf{S}}^{n+1,(i)}} \mathbf{R}^{n+1,(i)} \tag{34}$$

   where

$$\nabla_{\dot{\mathbf{S}}^{n+1,(i)}} (\cdot) = \left\{ \begin{array}{c} \frac{\partial (\cdot)}{\partial \dot{\mathbf{F}}^{n+1,(i)}} \\ \frac{\partial (\cdot)}{\partial \dot{\mathbf{C}}^{n+1,(i)}} \end{array} \right\} \tag{35}$$

(c) Solve the following linear system using the generalized minimal residual method algorithm

$$\mathbf{K}^{n+1,(i)}\Delta\dot{\mathbf{S}}^{n+1,(i)} = -\mathbf{R}^{n+1,(i)} \tag{36}$$

(d) Use $\Delta\dot{\mathbf{S}}^{n+1,i}$ to update the iterations

$$\dot{\mathbf{S}}^{n+1,(i)} = \dot{\mathbf{S}}^{n+1,(i-1)} + \Delta\dot{\mathbf{S}}^{n+1,(i)} \tag{37}$$

$$\mathbf{S}^{n+1,(i)} = \mathbf{S}^{n+1,(i-1)} + \gamma\Delta t_n\Delta\dot{\mathbf{S}}^{n+1,(i)} \tag{38}$$

The implementation of an adaptive time step reduces the computation time of the numerical simulations more than an order of magnitude compared with maintaining a constant time step. Further, it permits us to analyze the accuracy of the method, regarding the time integration. To define an adaptive time step, we make use of the fact that the generalized-α method transforms into the backward Euler method by setting $\gamma = \alpha_m = \alpha_f = 1$. Comparing the results from both methods, we are able to evaluate an error estimate e and to update the time-step size using the formula

$$F(e, \Delta t) = \rho\left(\frac{\Upsilon_{\Delta t}}{e}\right)^{\frac{1}{2}}\Delta t \tag{39}$$

where, according to the values suggested in [61], the safety coefficient ρ is set to 0.9 and the tolerance of the method $\Upsilon_{\Delta t}$ is set to 10^{-3}. Thus, for a certain time step n, we can implement a time-step size adaptive algorithm as follows:

Algorithm 1 Adaptive time-step size

Given: $\dot{\mathbf{S}}^n$, $\mathbf{S}^n$, and Δt_n,

1: Compute $\mathbf{S}_{BE}^{n+1}$ using backward Euler and Δt_n
2: Compute $\mathbf{S}_\alpha^{n+1}$ using generalized-α and Δt_n
3: Calculate $e_{n+1} = \frac{\|\mathbf{S}_{BE}^{n+1} - \mathbf{S}_\alpha^{n+1}\|}{\|\mathbf{S}_\alpha^{n+1}\|}$
4: **if** $e_{n+1} > \Upsilon_{\Delta t}$ **then**
5:     Recalculate time-step size $\Delta t_n \leftarrow F(e_{n-1}, \Delta t_n)$
6:     **goto** 1
7: **else**
8:     Update time-step size $\Delta t_{n+1} = F(e_{n+1}, \Delta t_n)$
9:     **continue**
10: **end if**

---

4. RESULTS AND DISCUSSION

In this section, we present some numerical results of our numerical method for the tumor angiogenesis model. We begin with the description of the development of a vascular network through a numerical example. We also show the effect of the time-step size adaptivity. We continue this section, presenting the influence of relevant parameters of the model in a parametric study. Finally, we conclude the section with an analysis of different examples with variations in the initial conditions.

4.1. Numerical example

We perform this numerical example on a square domain $\overline{\Omega} = [0, 300]^2$, which represents a tissue of 375 µm × 375 µm. We define a mesh composed by 256^2 quadratic elements that spans all the domain. The simulation implements the numerical method described in Section 3, including the adaptive time-stepping scheme presented in Algorithm 1.
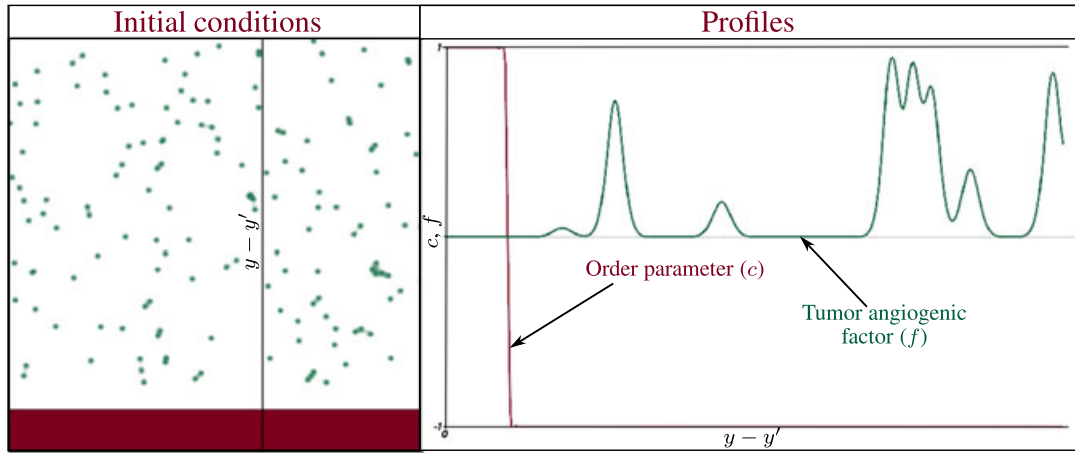
Figure 7. Initial conditions of the numerical examples of Figures 8 and 10. On the left-hand side is plotted a square domain ($\overline{\Omega} = [0, 300]^2$) that represents a tissue with an initial capillary at the bottom (red) and 200 randomly distributed hypoxic cells (green). The profiles of the order parameter and the tumor angiogenic factor along $y-y'$ are plotted on the right-hand side.

We establish the following initial conditions for this numerical example: The value of the order parameter is set to minus one, $c = -1$, in all the domain, except for a stripe of constant width at the bottom of the domain, where we set $c = 1$. This stripe represents a capillary. At the scale considered in this example, the average capillary width varies from 5 to 10 μm ([14]). In the simulations, we take 37.5 μm. At the beginning of the simulation $\Omega_{\text{TEC}}(t_0) = \emptyset$ and $\Omega_{\text{HYC}}(t_0) = \bigcup_{j=1}^{200} \Omega_{\text{HYC}}^j(t_0)$, where the $\mathbf{x}_{\text{HYC}}^j$, $j = 1, \ldots, 200$, are randomly distributed in Ω. We employ periodic boundary conditions in the horizontal direction and free flux conditions in the vertical direction.

The initial configuration described earlier, shown in Figure 7, simulates an avascular tumor and its environment in a tissue. The tissue is square, although the implementation of the periodic boundary conditions allows the vasculature and the TAF to spread horizontally without reaching the end of the domain in this direction. The tumor is modeled as 200 HYCs, Ω_{HYC}, and the environment is composed of host cells, $c = -1$, and endothelial cells forming a capillary, $c = 1$.

Figure 8 shows a numerical example at different times. The TAF produced by the HYCs diffuses from them throughout the domain, filling it. As the diffusible factor reaches the endothelial cells, they consume it. For a time lapse, there is a pseudo-equilibrium situation, in which all the domain is filled with TAF, and the TAF produced is consumed by the endothelial cells. This situation is maintained, until the factor pervades the capillary in a point with enough quantity to activate a TEC. Figure 8(b) presents several time steps after the pseudo-equilibrium is broken. The incipient capillary starts to take shape starting by a single cell followed by proliferative cells in the stalk of the sprout. The proliferation entails a consumption of the TAF that becomes more evident in Figure 8(c). The capillary continues growing, and new sprouts appear, forming branches (Figure 8(d, e)). During the simulation, the TECs find other endothelial cells in their growing direction. In these cases (see details in Figure 8(f, g)), they merge with another originating anastomosis. The growth and branching proceeds (Figure 8(h)) until all the HYCs become normoxic. This process creates a vascular pattern characteristic of tumor angiogenesis, shown in Figure 8(i).

Figure 9 shows the evolution of the time-step size, Δt, with respect to time, t. At the beginning of the simulation, the Δt is set to 10^{-4}. Then it follows an increasing trajectory, along which the time step, becoming larger. During this period, the dominating phenomenon is the diffusion of the TAF. Also, several new capillaries appear at the end of ascending slope, characterized by little descents in the time-step size. The time-step size acquires its maximum value in the vicinity of $t = 19$. From this point, the time-step curve presents a global descending trend with several fluctuations. This implies a deceleration of the numerical method related with the increment in complexity of the vascular network. The local minima of the fluctuations correspond to the creation of new sprouts.
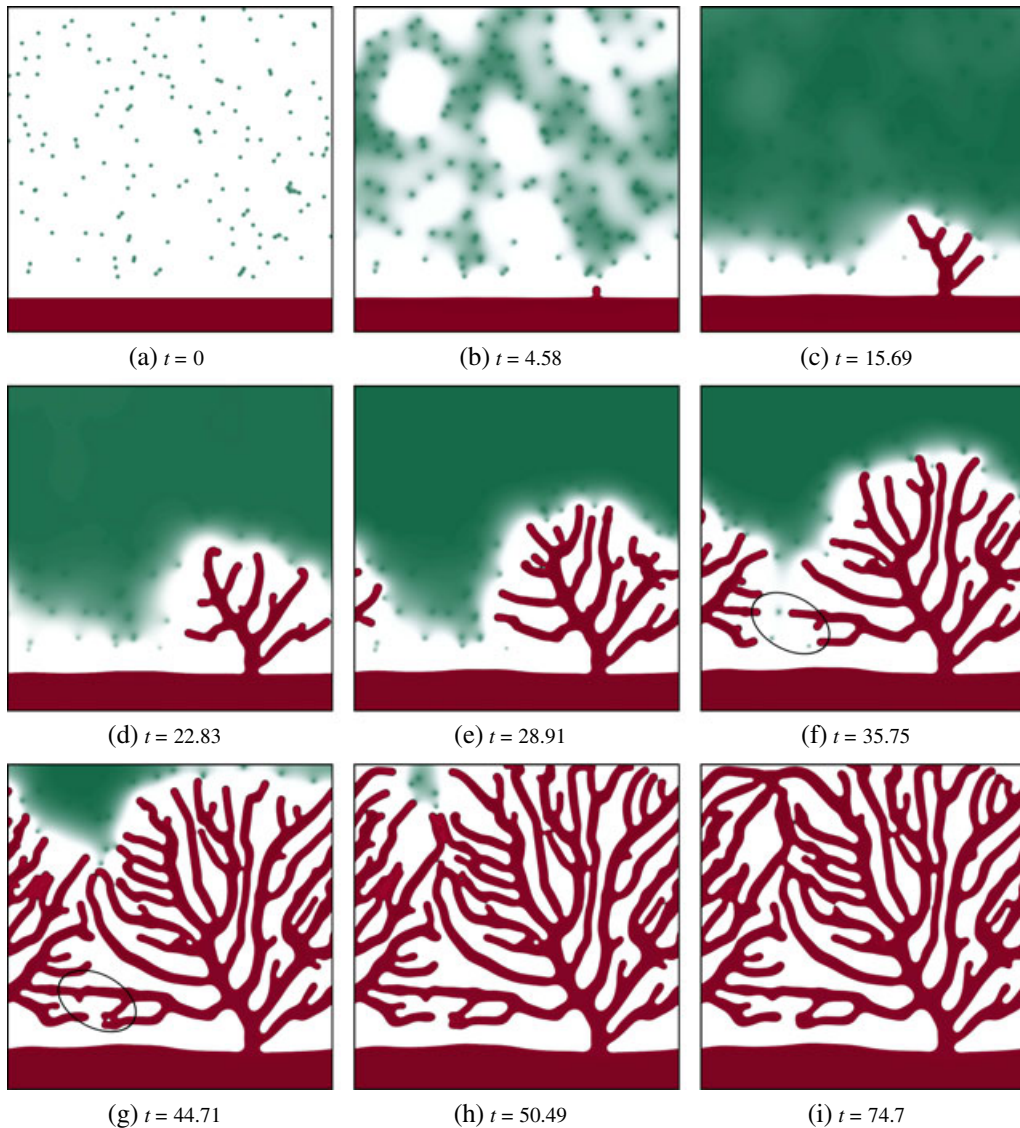
Figure 8. Formation of a vascular pattern at different times. The parameters used for this numerical example are those presented in Table I, and the domain is $\overline{\Omega} = [0, 300]^2$. The tumor angiogenic factor (green) is produced by randomly distributed hypoxic cells and promotes the growth of new capillaries (red) from the initial one situated at the bottom of the domain. In their growth, the capillaries fuse with another (anastomosis) as shown in the highlighted areas. The final pattern shows the disorganized sprouting and tortuous capillaries characteristic of tumor angiogenesis.

4.2. Parametric study of the model

Here, we present a study of two of the most biologically relevant parameters of the model: B_p, that controls the proliferation, and χ, that alters the chemotactic velocity. The characteristics of the domain size, mesh, and initial and boundary conditions are the same as those used for the numerical example in Section 4.1. All the parameters of the model, except those object of the study, maintain the values given in Table I.

We used our numerical method to perform nine simulations (Figure 10) in which the parameters take the following values: 50%, 100%, and 130% of B_p (as given in Table I) and 16%, 100%, and 200% of χ (as given in Table I). The disposition of the simulations is such that the one with lower proliferation and chemotactic velocity is in the bottom-left corner and the one with highest
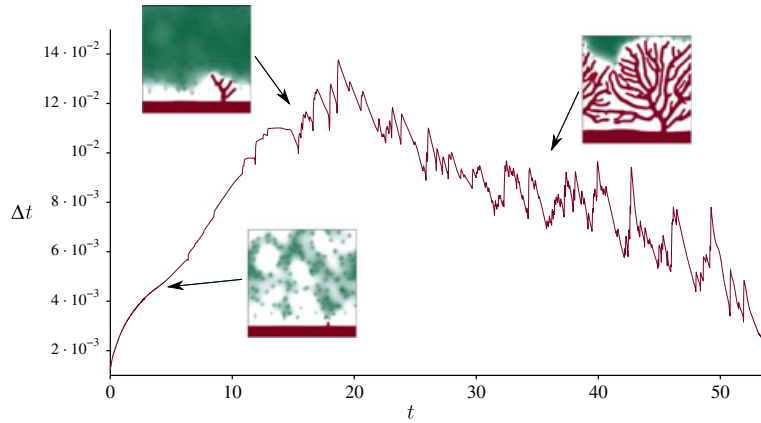
Figure 9. Evolution of the time-step size (Δt) with respect to time (t) of the numerical example of Figure 8 using the adaptive time-step Algorithm 1. The insets show the evolution of the capillary growth at different instants. The time-step size increases at the beginning when there are few new capillaries until a maximum around $t = 19$. From this point, the evolution of the time step is characterized by a decrease in its size due to an increment in the complexity in the capillaries pattern.
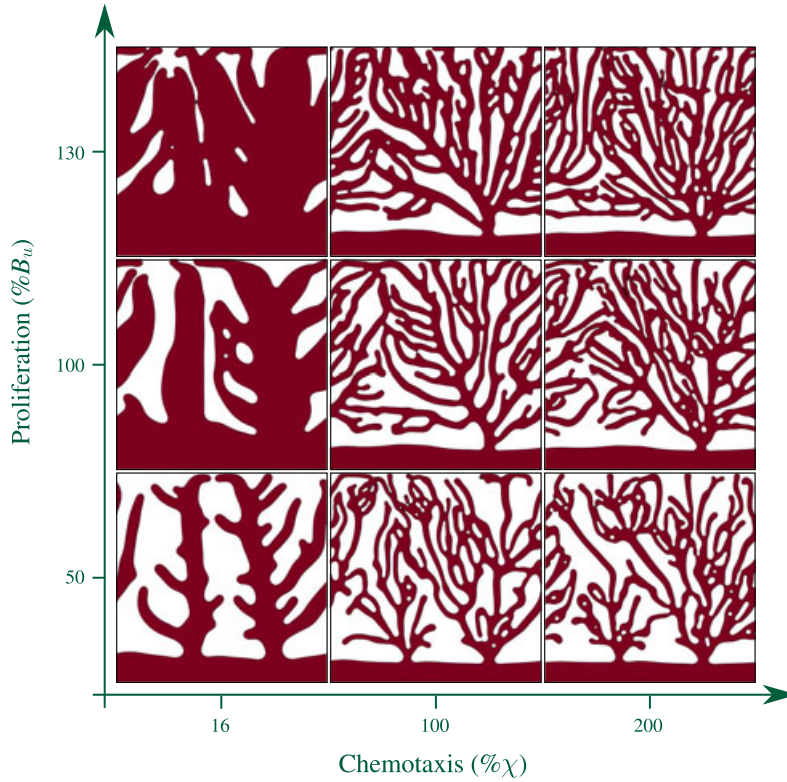

Figure 10. Parametric study of the model. Comparison of nine stationary patterns resulting from different parameter combinations. The value of the parameters is shown in the axis as a percentage of the proliferation (B_u) and chemotaxis (χ) from Table I. The nine patterns evolved from the same initial conditions defined in Figure 7.

parameter values is in the opposite corner. In the center of the grid is shown the final pattern of the numerical example of Section 4.1, which we take as reference point for comparison purposes.

The resulting vascular networks present different characteristic patterns. If we compare the simulations within the same row, we observe a decrease in the capillary width as the chemotactic velocity

increases. This behavior is produced by the fact that the SECs are provided with less time to proliferate. An analysis of the second column shows a variation in the capillary width driven by the proliferative parameter. As B_p increases, so does the width of the capillaries. Furthermore, these simulations show sparser patterns when the proliferation is low.

The difference in the patterns of the first column and the rest is remarkable. The low value of the chemotactic velocity, 16% of χ, gives rise to very wide capillaries. In addition, within this column, we can easily appreciate the influence of the proliferation rate. When it is low, the capillaries are over-dimensioned, but with well-defined boundaries. Conversely, they become a mass of endothelial cells that spans almost all the domain when the proliferation is high as shown in the top-left corner..

4.3. Influence of the hypoxic cell distribution and initial capillaries

We study the influence of HYCs distribution and initial capillaries by performing several simulations on the domain $\overline{\Omega} = [0, 700]^2$, which represents a tissue of 875 μm × 875 μm. Note that the surface of the domain is approximately 5.4 times larger than that of the previous examples. However, we use the same mesh composed by 256^2 quadratic elements. We implement our numerical method and the adaptive time-step scheme given in Algorithm 1. As initial conditions, we set diverse capillary configurations, maintaining the width of the vessels to 37.5 μm. The location of the initial HYCs is random and different between the numerical examples. The TAF is initially zero in $\Omega \backslash \Omega_{HYC}(t_0)$, and there are no TECs at the beginning of the simulations; therefore, $\Omega_{TEC}(t_0) = \emptyset$.

We present in Figure 11 the results of four different numerical examples with an initial capillary at the bottom of each domain. There are 200 HYCs randomly distributed in the domain according to a uniform density function. The objective of these simulations is twofold. On the one hand, we can perform an analysis of the different patterns formed under the influence of diverse initial HYCs. From Figure 11, we may conclude that the final patterns hold similar characteristics, regarding the width of capillaries, the number of branches, and the density of the pattern. We observe differences in the distance between the sprouts that grow from the main initial capillary. Usually, the growth from the initial capillary occurs when the pseudo-equilibrium situation mentioned in Section 4.1
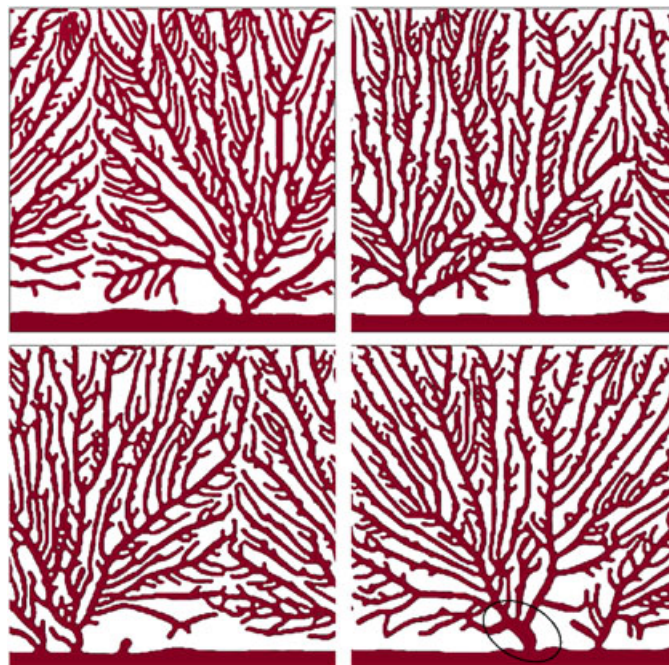

Figure 11. Numerical examples of the model with different randomly distributed hypoxic cells on the domain $\overline{\Omega} = [0, 700]^2$. The patterns present similar characteristics in all four simulations regarding the width and number of capillaries and the density of the network.

is broken. Thereafter, no additional capillaries originated from the initial one. In addition, in the bottom-right plot, the first part of the highlighted capillary is wider than that of the rest. This situation is caused by several initial HYCs gathered in a small region and surrounded by an empty zone.

On the other hand, these simulations serve as proof for the accuracy of the method. We used the same mesh as in Section 4.1 for a domain with a surface approximately 5.4 times larger. Nevertheless, the numerical method is still able to capture the more complex vascular pattern with accuracy.

Figure 12 shows three numerical examples. We performed each of the simulations with different initial conditions for the HYC distribution and the initial capillaries. We show these initial configurations on the left-hand side of Figure 12, whereas the correspondent final results are shown on the right-hand side. For the simulation in the first row, we choose a circular initial capillary surrounding 200 HYCs randomly distributed in the domain according to a uniform density function. This configuration could be interpreted as a two-dimensional approach of an *in vivo* assay of angiogenesis in a cornea [62, 63], at a different scale. The circular capillary would be equivalent to the corneal limbus,
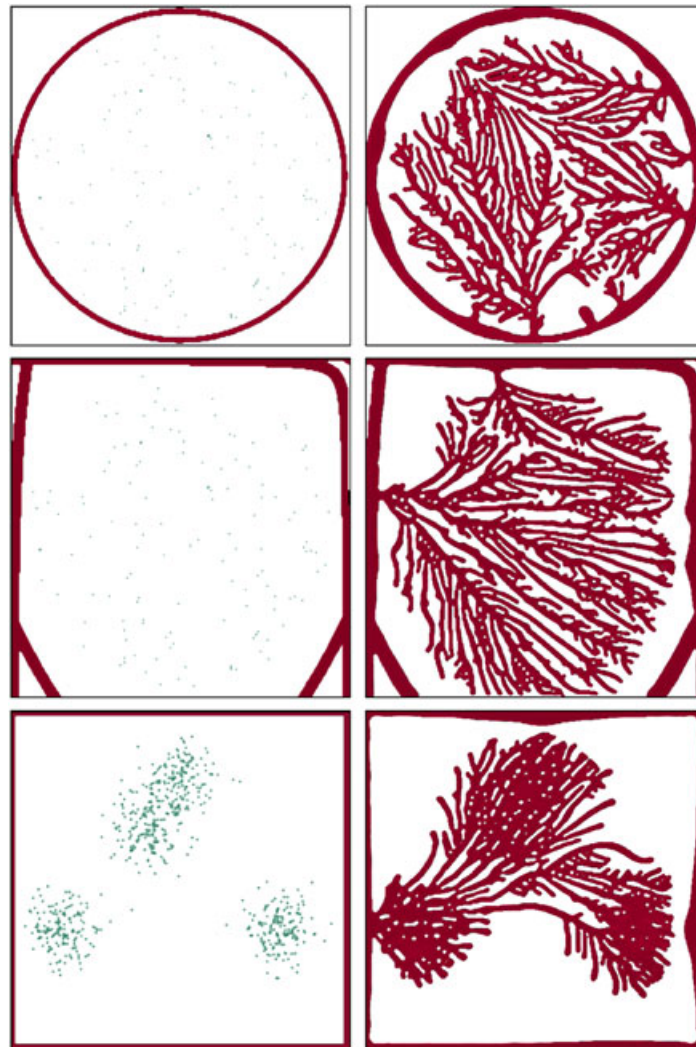

Figure 12. Initial conditions (left) and final patterns (right) of three simulations. The first row presents a circular initial capillary, the second represents a more real configuration of several capillaries in a tissue, and the third shows a multifocal distribution of hypoxic cells. The three simulations were performed on the domain $\overline{\Omega} = [0, 700]^2$.

and the space inside with the HYCs would be the avascular retina with cancerous cells. Additionally, the configuration could also be compared with the vascular growth of a tumor implanted in the dorsal skin of a mouse, observed through intravital microscopy [64], with no previous capillaries in the observed domain. The final network of this configuration is formed by three main capillaries grown from the circular one that branch as they become closer to the HYCs.

In the second row of Figure 12, we present a simulation in which the 200 HYCs are the same as in the previous row, but the initial capillaries are different. Instead of geometric shapes, we create a more likely approach to an initial vascular network in a real tissue. The resulting pattern covers the positions of the HYCs.

Finally, we present in the last row of Figure 12 a configuration with four initial capillaries, each of them in one boundary of the domain. In addition, we choose a distribution of HYCs on the basis of four normal density functions. Thus, the initial conditions of this simulation mimic those of a multifocal tumor in a tissue. This result shows how the model is able to create vascular patterns for each of the foci.

5. CONCLUSIONS

The dynamics of tumor angiogenesis and its impact on cancer growth remain as fundamental open problems in cancer biology. We derive an algorithmic framework for a hybrid model that couples cellular-scale kinetics and an averaged phase-field description at the macroscale. We formulate the discrete cellular kinetics into a functional framework that permits an efficient numerical treatment of the coupled problem. We perform several numerical simulations by using our algorithms. The examples show the accuracy and efficiency of the method in a number of physically relevant situations. Our simulations provide insight into the dynamics of the governing equations and the underlying biological process behind them.

6. SUPPORTING INFORMATION

Supporting information‡ includes four movies that can be found online at www.interscience.wiley.com

1. Video S1: Formation of the capillary network of Figure 8. Two hundred randomly distributed HYCs on a domain $\overline{\Omega} = [0, 300]^2$ promote the growth of the vasculature by means of the TAF.
2. Video S2: Formation of the capillary network whose final pattern is presented in the top-left plot of Figure 11. The domain of this simulation is $\overline{\Omega} = [0, 700]^2$, approximately 5.4 times the size of the domain in Figure 8.
3. Video S3: Formation of the capillary network from an initial circular capillary on the domain $[0, 700]^2$. This movie corresponds to the simulation shown in the first row of Figure 12.
4. Video S4: Formation of the capillary network of the simulation presented in the third row of Figure 12. Angiogenesis is promoted by four groups of HYCs as in a multifocal tumor.

REFERENCES

1. Conway EM, Collen D, Carmeliet P. Molecular mechanisms of blood vessel growth. *Cardiovascular Research* 2001; **49**(3):507–521.

‡All Supporting Information may be found in the online version of this article.

2. Kurz H, Burri PH, Djonov VG. Angiogenesis and vascular remodeling by intussusception: from form to function. *News in Physiological Sciences* 2003; **18**(2):65–70.
3. Figg WD, Folkman J. *Angiogenesis: An Integrative Approach from Science to Medicine*. Springer: New York, 2011.
4. Breier G. Angiogenesis in embryonic development—a review. *Placenta* 2000; **21**(Suppl. 1):S11–S15.
5. Tonnesen MG, Feng X, Clark RA. Angiogenesis in wound healing. *Journal of Investigative Dermatology Symposium Proceedings* 2000; **5**(1):40–46.
6. Carmeliet P, Jain RK. Angiogenesis in cancer and other diseases. *Nature* 2000; **407**(6801):249–257.
7. Folkman J. Tumor angiogenesis: therapeutic implications. *The New England Journal of Medicine* 1971; **285**(21):1182–1186.
8. Hanahan D, Weinberg RA. The hallmarks of cancer. *Cell* 2000; **100**(1):57–70.
9. Hanahan D, Weinberg RA. Hallmarks of cancer: the next generation. *Cell* 2011; **144**(5):646–674.
10. Hellström M, Phng LK, Hofmann JJ, Wallgard E, Coultas L, Lindblom P, Alva J, Nilsson AK, Karlsson L, Gaiano N, Yoon K, Rossant J, Iruela-Arispe ML, Kalén M, Gerhardt H, Betsholtz C. Dll4 signalling through notch1 regulates formation of tip cells during angiogenesis. *Nature* 2007; **445**(7129):776–780.
11. Gerhardt H, Golding M, Fruttiger M, Ruhrberg C, Lundkvist A, Abramsson A, Jeltsch M, Mitchell C, Alitalo K, Shima D, Betsholtz C. VEGF guides angiogenic sprouting utilizing endothelial tip cell filopodia. *Journal of Cell Biology* 2003; **161**(6):1163–1177.
12. Baluk P, Hashizume H, McDonald DM. Cellular abnormalities of blood vessels as targets in cancer. *Current Opinion in Genetics & Development* 2005; **15**(1):102–111.
13. Folkman J, Kalluri R. *Holland-Frei cancer medicine*, (6 edn), Tumor Angiogenesis. Hamilton (ON): BC Decker, 1984; 161–194.
14. Shiu YT, Weiss JA, Hoying JB, Iwamoto MN, Joung IS, Quam CT. The role of mechanical stresses in angiogenesis. *Critical Reviews in Biomedical Engineering* 2005; **33**(5):431–510.
15. Krishnan L, Underwood CJ, Maas S, Ellis BJ, Kode TC, Hoying JB, Weiss JA. Effect of mechanical boundary conditions on orientation of angiogenic microvessels. *Cardiovascular Research* 2008; **78**(2):324–332.
16. Xiong G, Figueroa CA, Xiao N, Taylor CA. Simulation of blood flow in deformable vessels using subject-specific geometry and assigned variable mechanical wall properties. *International Journal for Numerical Methods in Biomedical Engineering* 2010; **27**(7):1000–1016.
17. Anderson ARA, Chaplain MAJ. A mathematical model for capillary network formation in the absence of endothelial cell proliferation. *Applied Mathematics Letters* 1998; **11**(3):109–114.
18. Orme ME, Chaplain MAJ. Two-dimensional models of tumour angiogenesis and anti-angiogenesis strategies. *Mathematical Medicine and Biology* 1997; **14**(3):189–205.
19. Levine HA, Sleeman BD, Nilsen-Hamilton M. Mathematical modeling of the onset of capillary formation initiating angiogenesis. *Journal of Mathematical Biology* 2001; **42**(3):195–238.
20. Sun S, Wheeler MF, Obeyesekere M, Patrick CW. A deterministic model of growth factor-induced angiogenesis. *Bulletin of Mathematical Biology* 2005; **67**(2):313–337.
21. Frieboes HB, Jin F, Chuang YL, Wise SM, Lowengrub JS, Cristini V. Three-dimensional multispecies nonlinear tumor growth—II: tumor invasion and angiogenesis. *Journal of Theoretical Biology* 2010; **264**(4):1254–1278.
22. Bentley K, Mariggi G, Gerhardt H, Bates PA. Tipping the balance: robustness of tip cell selection, migration and fusion in angiogenesis. *PLoS Computational Biology* 2009; **5**(10):e1000 549.
23. Capasso V, Morale D. Stochastic modelling of tumour-induced angiogenesis. *Journal of Mathematical Biology* 2009; **58**(1-2):219–233.
24. Macklin P, McDougall S, Anderson ARA, Chaplain MAJ, Cristini V, Lowengrub JS. Multiscale modelling and nonlinear simulation of vascular tumour growth. *Journal of Mathematical Biology* 2009; **58**(4–5):765–798.
25. Milde F, Bergdorf M, Koumoutsakos P. A hybrid model for three-dimensional simulations of sprouting angiogenesis. *Biophysical Journal* 2008; **95**(7):3146–3160.
26. Travasso RDM, Poiré EC, Castro M, Rodríguez-Manzaneque JC, Hernández-Machado A. Tumor angiogenesis and vascular patterning: a mathematical model. *PLoS One* 2011; **6**(5):e19 989.
27. Chen LQ. Phase-field models for microstructure evolution. *Annual Review of Materials Science* 2002; **32**:113–140.
28. Emmerich H. *The Diffuse Interface Approach in Materials Science*, Lecture Notes in Physics, Vol. 73. Springer: Berlin Heidelberg, 2003.
29. Kobayashi R. A numerical approach to three-dimensional dendritic solidification. *Experimental Mathematics* 1994; **3**(1):59–81.
30. Gomez H, Calo VM, Bazilevs Y, Hughes TJR. Isogeometric analysis of the Cahn–Hilliard phase-field model. *Computational Methods in Applied Mechanics and Engineering* 2008; **197**(49–50):4333–4352.
31. Gomez H, Hughes TJR. Provably unconditionally stable, second-order time-accurate, mixed variational methods for phase-field models. *Journal of Computational Physics* 2011; **230**:5310–5327.
32. Cueto-Felgueroso L, Juanes R. A phase field model of unsaturated flow. *Water Resources Research* 2009; **45**:W10 409.
33. Nonomura M. Study on multicellular systems using a phase field model. *PLoS ONE* 2012; **7**(4):e33 501.
34. Campelo F, Hernández-Machado A. Dynamic model and stationary shapes of fluid vesicles. *European Physical Journal E* 2006; **20**(1):37–45.
35. Cristini V, Li X, Lowengrub JS, Wise SM. Nonlinear simulations of solid tumor growth using a mixture model: invasion and branching. *Journal of Mathematical Biology* 2009; **58**:723–763.

36. Tinsley Oden J, Hawkins-Daarud A, Prudhomme S. General diffuse-interface theories and an approach to predictive tumor growth modeling. *Mathematical Models and Methods in Applied Sciences* 2010; **20**(03):477–517.

37. Frieboes HB, Lowengrub JS, Wise SM, Zheng X, Macklin P, Bearer EL, Cristini V. Computer simulation of glioma growth and morphology. *NeuroImage* 2007; **37**(Suppl. 1):S59–S70.

38. Wise SM, Lowengrub JS, Frieboes HB, Cristini V. Three-dimensional multispecies nonlinear tumor growth—I: model and numerical method. *Journal of Theoretical Biology* 2008; **253**(3):524–543.

39. Ye X, Cheng X. The Fourier spectral method for the Cahn–Hilliard equation. *Applied Mathematics and Computation* 2005; **171**(1):345–357.

40. Stogner RH, Carey GF. C1 macroelements in adaptive finite element methods. *International Journal for Numerical Methods in Engineering* 2007; **70**(9):1076–1095.

41. Hawkins-Daarud A, van der Zee KG, Tinsley Oden J. Numerical simulation of a thermodynamically consistent four-species tumor growth model. *International Journal for Numerical Methods in Biomedical Engineering* 2012; **28**(1):3–24.

42. Xia Y, Xu Y, Shu CW. Local discontinuous Galerkin methods for the Cahn–Hilliard type equations. *Journal of Computational Physics* 2007; **227**(1):472–491.

43. Engel G, Garikipati K, Hughes TJR, Larson MG, Mazzei L, Taylor RL. Continuous/discontinuous finite element approximations of fourth-order elliptic problems in structural and continuum mechanics with applications to thin beams and plates, and strain gradient elasticity. *Computer Methods in Applied Mechanics and Engineering* 2002; **191**(34):3669–3750.

44. Cyron CJ, Arroyo M, Ortiz M. Smooth, second order, non-negative meshfree approximants selected by maximum entropy. *International Journal for Numerical Methods in Engineering* 2009; **79**(13):1605–1632.

45. Arroyo M, Ortiz M. Local maximum-entropy approximation schemes: a seamless bridge between finite elements and meshfree methods. *International Journal for Numerical Methods in Engineering* 2006; **65**(13):2167–2202.

46. Rosolen A, Millán D, Arroyo M. Second-order convex maximum entropy approximants with applications to high-order pde. *International Journal for Numerical Methods in Engineering* 2013; **94**(2):150–182.

47. Hughes TJR, Cottrell JA, Bazilevs Y. Isogeometric analysis: CAD, finite elements, NURBS, exact geometry and mesh refinement. *Computer Methods in Applied Mechanics and Engineering* 2005; **194**(39–41):4135–4195.

48. Cottrell JA, Hughes TJR, Reali A. Studies of refinement and continuity in isogeometric structural analysis. *Computer Methods in Applied Mechanics and Engineering* 2007; **196**(41–44):4160–4183.

49. Bazilevs Y, Calo VM, Cottrell JA, Evans JA, Hughes TJR, Lipton S, Scott MA, Sederberg TW. Isogeometric analysis using T-splines. *Computer Methods in Applied Mechanics and Engineering* 2010; **199**(5-8):229–263.

50. Cottrell JA, Reali A, Bazilevs Y, Hughes TJR. Isogeometric analysis of structural vibrations. *Computer Methods in Applied Mechanics and Engineering* 2006; **195**(41–43):5257–5296.

51. Hughes TJR, Reali A, Sangalli G. Efficient quadrature for NURBS-based isogeometric analysis. *Computer Methods in Applied Mechanics and Engineering* 2010; **199**(5–8):301–313.

52. Auricchio F, Beirão da Veiga L, Hughes TJR, Reali A, Sangalli G. Isogeometric collocation for elastostatics and explicit dynamics. *Computer Methods in Applied Mechanics and Engineering* 2012; **249–252**:2–14.

53. Buffa A, Sangalli G, Vázquez R. Isogeometric analysis in electromagnetics: B-splines approximation. *Computer Methods in Applied Mechanics and Engineering* 2010; **199**(17-20):1143–1152.

54. Schillinger D, Dedè L, Scott MA, Evans JA, Borden MJ, Rank E, Hughes TJR. An isogeometric design-through-analysis methodology based on adaptive hierarchical refinement of NURBS, immersed boundary methods, and T-spline cad surfaces. *Computer Methods in Applied Mechanics and Engineering* 2012; **249-252**:116–150.

55. Lipton S, Evans J, Bazilevs Y, Elguedj T, Hughes TJR. Robustness of isogeometric structural discretizations under severe mesh distortion. *Computer Methods in Applied Mechanics and Engineering* 2010; **199**(5–8):357–373.

56. Gomez H, Hughes TJR, Nogueira X, Calo VM. Isogeometric analysis of the isothermal Navier–Stokes–Korteweg equations. *Computer Methods in Applied Mechanics and Engineering* 2010; **199**(25–28):1828–1840.

57. Gomez H, Nogueira X. An unconditionally energy-stable method for the phase field crystal equation. *Computer Methods in Applied Mechanics and Engineering* 2012; **249–252**:52–61.

58. Gomez H, París J. Numerical simulation of asymptotic states of the damped Kuramoto–Sivashinsky equation. *Physical Review E* 2011; **83**:046702.

59. Emmerich H. Advances of and by phase-field modelling in condensed-matter physics. *Advances in Physics* 2008; **57**(1):1–87.

60. Hawkins-Daarud A, Prudhomme S, van der Zee KG, Tinsley Oden J. Bayesian calibration, validation, and uncertainty quantification of diffuse interface models of tumor growth. *Journal of Mathematical Biology* 2012:1–29.

61. Lang J. Two-dimensional fully adaptive solutions of reaction-diffusion equations. *Applied Numerical Mathematics* 1995; **18**(1–3):223–240.

62. Kenyon BM, Voest EE, Chen CC, Flynn E, Folkman J, D'Amato RJ. A model of angiogenesis in the mouse cornea. *Investigative Ophthalmology & Visual Science* 1996; **37**(8):1625–1632.

63. Muthukkaruppan VR, Kubai L, Auerbach R. Tumor-induced neovascularization in the mouse eye. *Journal of the National Cancer Institute* 1982; **69**(3):699–708.

64. Jain RK, Munn LL, Fukumura D. Dissecting tumour pathophysiology using intravital microscopy. *Nature Reviews Cancer* 2002; **2**(4):266–276.